A facile synthesis of Mn_3O_4/Fe_3O_4 superparamagnetic nanocomposites by chemical precipitation: Characterization and application in dye degradation

Gabriela C. Silva [a,c], Virginia S.T. Ciminelli [a,c,*], Angela M. Ferreira [b,c], Nathalia C. Pissolati [b,c], Paulo Renato P. Paiva [c], Jorge L. López [d]

[a] Department of Metallurgical and Materials Engineering, Universidade Federal de Minas Gerais (UFMG), Av. Antonio Carlos, 6627, Pampulha, 31270901 Belo Horizonte, Minas Gerais, Brazil
[b] Department of Chemistry, Centro Federal de Educação Tecnológica de Minas Gerais (CEFET-MG), Av. Amazonas, 5253, Nova Suíça, 30421-169 Belo Horizonte, Minas Gerais, Brazil
[c] National Institute of Science and Technology on Mineral Resources, Water and Biodiversity (INCT-Acqua), Brazil
[d] Centro de Ciências Biológicas e Da Natureza, Universidade Federal do Acre (UFAC), Rio Branco, AC 69915-900, Brazil

ARTICLE INFO

ABSTRACT

Degradation of methylene blue (MB) is investigated using Mn_3O_4 as an oxidant. Discrete Mn_3O_4 particles and Mn_3O_4/Fe_3O_4 nanocomposites are synthesized via coprecipitation by using air as an oxidant in the absence and presence of previously synthesized magnetite nanoparticles, respectively. Characterization results show that superparamagnetic magnetite nanoparticles of $\sim$10 nm were synthesized. The Mn_3O_4 synthesis in the presence of these magnetite nanoparticles favors the formation of a pure, highly ordered Mn_3O_4/Fe_3O_4 superparamagnetic nanocomposite, which can be separated by an external magnetic field. This nanocomposite is applied to the oxidative decolorization of methylene blue (MB) and is capable of catalyzing the complete N-demethylation of MB, forming thionine as the final product and removing 93% of the dye in approximately 1 h.

1. Introduction

Water pollution is one of the major challenges faced by global society. The development of new materials and methods for water treatment has received growing interest as a remedy for environmental problems. Dye waste is an important source of water contamination since the presence of dyes in water reduces light penetration, hindering photosynthesis in aquatic plants, not to mention the undesirable coloring of streams. Many textile industries use dyes generating a colored wastewater that causes damage to the ecological system. Therefore, treating dye effluents prior to their discharge is essential [1]. Manganese oxides are powerful oxidants due to their relatively high reducing potential (Fig. S1). It has already been reported that Mn^{3+} and Mn^{4+} oxides and hydroxides can oxidize many inorganic and organic compounds [2–6]. Mn_3O_4 (hausmannite) is a spinel oxide of Mn

containing both di- and tri-valent manganese that presents high standard redox potential ($E_h^{298} = 1.824$ V) in the reduction to Mn^{2+}. In view of the strong oxidative characteristic, Mn_3O_4 has been evaluated as an effective oxidant for the degradation of dyes in water, since oxidation of dyes usually requires the use of strong electron acceptors with standard reducing potential higher than 1.0 V [7–9]. The introduction of magnetic properties in Mn_3O_4 can improve its separation from dye-tainted effluents. Magnetic materials can be conveniently recovered by magnetic separation, in turn avoiding the filtration steps, which represent a barrier to the application of high performance, small-sized materials in environmental remediation processes and the treatment of large volumes of aqueous solutions. To address this problem, magnetite nanoparticles are being combined with other compounds or covered by an active compound [10–12]. In both cases, the magnetic property of magnetite is preserved. Only a few studies have focused on magnetic manganese oxide composites for use in water treatment [11–14]. Most of these studies focus on manganese dioxides and only one investigates manganese oxides with high standard reducing potential, such as Mn_3O_4 and Mn_2O_3 [11,13,14]. However, in the aforementioned work, the Mn_3O_4 and Mn_2O_3 are synthesized using high temperature (250 °C) and long

* Corresponding author at: Universidade Federal de Minas Gerais (UFMG), Av. Antonio Carlos, 6627, Pampulha, 31270901 Belo Horizonte, Minas Gerais, Brazil. Tel.: +55 3134091812; fax: +553134091817.
E-mail address: ciminelli@demet.ufmg.br (Virginia S.T. Ciminelli).

reaction time (24 h). Furthermore, the combined effect of oxidation/sorption is not investigated.

Given that context, the present work addresses the development a simplified synthesis method (temperature, reagents, time) of magnetic composites with a manganese oxide of high standard reducing potential, such as Mn_3O_4. Moreover, the investigation of their combined oxidation/sorption properties in stirred, solid-aqueous environmental systems to remove both inorganic and organic contaminants is a subject of relevance. Here, we report the application in methylene blue degradation of a magnetic composite based on Mn_3O_4 synthesized at room temperature and using air as an oxidant.

2. Materials and methods

All chemicals were of analytical grade and used without further purification. All solutions were prepared with deionized water with a conductivity of 18.2 μS/cm obtained with a Milli-Q water purification system (Millipore). To remove contaminants that had been potentially adsorbed onto the glass and plastic walls, all vessels and instruments were cleaned by soaking in detergent solution, then in 1.0 mol/L HNO_3 solution, and subsequently in deionized water, in each case for at least 24 h. All parts of the spectroscopic equipment used to extract and fill the sample were cleaned and rinsed properly with acetone. The pH electrode (713 pH Meter, Metrohm) was calibrated prior to use with three pH buffers (pH 4.0, 7.0, and 10.0).

2.1. Synthesis of magnetite nanoparticles (mag)

Magnetite particles were prepared by a chemical precipitation route. An aqueous solution prepared with 400 mL of deionized water, 9.61 g of $Fe_2(SO_4)_3 \cdot 5H_2O$ (97%, Aldrich), 7.13 g of $FeSO_4 \cdot 7H_2O$ (RegentPlus^{TM}, ≥99% – Aldrich) and 100 mL of a 5.0 mol/L KOH (Sigma–Aldrich) solution was stirred under N_2 atmosphere at 70 °C for 2 h. The black suspension was filtered, washed with water several times, and finally dried in an oven at 45 °C [15–17].

2.2. Synthesis of magnetic Mn_3O_4 composite (Mnmag)

The composite was prepared by placing 1000 mL of deionized water in contact with 0.5 g of previously synthesized magnetite nanoparticles and 45 mL of 1.0 mol/L $MnCl_2 \cdot 4H_2O$ (Sigma–Aldrich) solution at pH 12 (1.0 mol/L KOH – Sigma–Aldrich) in a 2000 mL Pyrex beaker under stirring (mechanical stirrer, Fisatom 713 D) and constant air input (aquarium pump power 500) for 30 min. The same reaction was also carried out in the absence of magnetite nanoparticles for comparison. A brown colored solid was separated from solution by a neodymium magnet (180 mm × 100 mm × 35 mm, Imatec Produtos Magnéticos Ltda), washed with deionized water solution and dried in a dessicator at room temperature.

2.3. Methylene blue (MB) degradation

Decolorization experiments were conducted in a glass beaker, typically containing 68 mL of 1.4×10^{-5} mol/L MB dye solution and 50 mg of Mn_3O_4 nanoparticles and Mn_3O_4 magnetic composite. The mixture was allowed to react at room temperature under stirring. The progress of decolorization was assessed by UV–vis spectroscopic measurements of the mixture at different time intervals (5 min to 3 h). Some aliquots were taken, centrifuged and filtered before spectrometric analysis. To investigate the effect of pH on the decolorization process, the experiment was performed at pH 3.0, 4.0 and 6.0 keeping the amount of Mn_3O_4 and the dye constant. The effect of duplicating and reducing the composite

mass was also investigated (25 and 100 mg of Mnmag). The tests were conducted in duplicate. Absorbance ranging from 0.3 to 1.0 is less susceptible to stray light and noise problems and hence becomes the preferred absorbance range for UV–vis analyses. Therefore, the MB concentration was chosen to obtain initial absorbance of 1.0.

2.4. Analysis instruments

Raman spectroscopic and X-ray diffraction (XRD) analyses were carried out for solid identification. Raman spectra were collected on a Horiba Jobin Yvon LABRAM-HR 800 spectrograph, equipped with a 633 nm helium–neon laser, 20 mW of power, attached to an Olympus BHX microscope equipped with 10×, 50×, and 100× lenses. Raman-scattered radiation was collected with 600 g/mm grating, in a 180° backscattering configuration. The spectra were collected in a frequency range of 100 to at least 1100 cm^{-1} with a step size of 1.1 cm^{-1}. A N_2 cooled charge couple device (CCD) detector was used to suppress extra noise and obtain sufficiently accurate results. To reduce noise ratio, spectra were acquired at acquisition times of 3 min twenty times.

The diffractograms were obtained on a Shimadzu 7000 X-ray diffractometer, using a copper anode (Cu Kα$_1$ radiation) and graphite crystal monochromator. Analyses were run by step-scanning from 4° to 90° 2θ, increments of 0.02 2θ and count time of 3 s. The Rietveld refinement was performed using the GSAS 2001 software and the EXPGUI interface. The function of the pseudo-Voigt profile of Thompson-Cox-Hastings was used and the background was adjusted by the Chebyschev polynomial. The scale factor, unit cell, background, asymmetric profile, parameters of the full width at half-height from the instrumental broadening (obtained with a standard atomic position), isotropic atomic displacements and occupation factors of cations were refined. The difference between the theoretical (calculated profile) and experimental (mineral phase) diffractograms was good, as demonstrated by the residual curves and by the small values of χ^2 (GOF-values). The values are: $\chi^2 = 1.440\%$ for sample mag, $\chi^2 = 1.265\%$ for sample Mnmag and $\chi^2 = 2.224\%$ for sample Mn_3O_4. The crystallite size was estimated using the crystallite size/lattice strain calculation (Williamson–Hall method) software for Shimadzu X-ray diffractometer. The Williamson–Hall equation is as follows (Eq. (1)):

$$\frac{\beta \cos\theta}{\lambda} = \frac{1 + 2\eta}{\varepsilon} \frac{\sin\theta}{\lambda} \tag{1}$$

where θ is the Bragg angle, β is the expanse of the diffraction line width (integral width), ε is the average size of crystal particles, λ is the wavelength of the X-ray and η is the grating distortion. The particle size in the direction perpendicular to the (h k l) plane is $D_{h k l} = K\varepsilon$, where K is the Scherrer's constant which is different depending on the crystal (1.05 is typical). Using these equations, the average crystallite size, d_{XRD}, is calculated. The β value to be substituted for this Equation is the value obtained by correcting the integral width according to the integral width curve using the "Jones Correction" method by which the inherent expansion of the system is corrected.

A Perkin Elmer, Paragon 1000 spectrometer was used for FTIR spectra collection. The sample scans ranged from 400 to 4000 cm^{-1} with 4.0 cm^{-1} resolution and were obtained as 128 scans. IR spectra were obtained as dry samples mixed with KBr corresponding to 8 mg of sample in approximately 40 mg of spectral grade KBr.

Mössbauer spectroscopy data were collected on a conventional constant acceleration Mössbauer spectrometer (Halder) in transmission mode with a ^{57}Co (Rh) source to identify the composite's magnetic phase. An iron metal sheet with a thickness of 25 μm was

used as calibration standard of the Mössbauer spectra. The amount of sample in the sample holder used in both samples was 30 mg/cm^2. The room-temperature spectra are complicated and fitting does not provide a unique set of parameters. The spectra were simulated using a model of superparamagnetic relaxation of two levels (spin ½) and stochastic theory. It was taken into account that the particles size distribution obeys a log-normal distribution [18]. A typical room temperature measurement of the magnetization vs. applied magnetic field was obtained with a vibrating sample magnetometer.

Transmission electron microscopy (TEM) images of the samples were obtained using a Tecnai-G2-20-FEI 2006 microscope equipped with a silicon–lithium energy dispersive spectroscopy (EDS) detector (EDAX) in the Center of Microscopy at the Universidade Federal de Minas Gerais (UFMG). Samples were prepared by dispersing the powdery material onto a lacy carbon film supported by a Cu grid. Selected area electron diffraction (SAED) was carried out in order to identify the presence of both Mn_3O_4 and Fe_3O_4 phases. The SAED pattern was indexed using JEMS software.

Measurements of the specific surface area were made by the BET (Brunauer–Emmett–Teller) – Multipoint method using a nitrogen gas sorption analyzer NOVA 1000 Quantachrome. Prior to measurement, the samples were weighed, degassed by placing them into a glass cell under vacuum for at least 24 h at 100 °C, and weighed again. For the composite and the Mn_3O_4 samples, mass loss upon outgassing was approximately 3%, and for magnetite, the mass loss was approximately 5%. The BET analyzer's Dewar flask was filled with liquid nitrogen and set into place. Each degassed sample was loaded and the results of the analysis collected.

3. Results and discussion

3.1. Characterization of the magnetic nanocomposite

Raman and FTIR spectroscopy results confirm that the magnetite particles (mag) synthesis was well performed (Fig. 1). Sample mag shows a pronounced Raman band at 672 cm^{-1} attributed to the A_{1g} vibrational mode of magnetite and two weak bands at 316 cm^{-1} and 546 cm^{-1} assigned to the T_{1g} vibrational mode of magnetite (Fig. 1a) [19]. Moreover, sample mag shows two broad FTIR absorption bands (Fig. 1b) centered at about 575 cm^{-1} and 400 cm^{-1} also related to magnetite [15]. Powder X-ray diffraction (XRD) pattern of sample mag is typical of single phase spinel oxides and shows broad peaks that correspond to a cubic

spinel structure of magnetite (Fe_3O_4) (Fig. 2a). The structure has been refined (Rietveld refinement, GSAS 2001) in the cubic space group, $Fd\bar{3}m$, and has the following cell parameters: lattice constant, a_0 = 8.3617 Å, and cell volume, V = 584.645 Å^3 (Fig. 2a). The sample presents crystallite size d_{XRD} calculated with Hall's equation of 13 nm (Table 1), in agreement with those estimated by TEM images (Fig. 3a). The lattice constant of the magnetite nanocrystals reveals a significant change of unit cell dimension. The typical value for the lattice constant of stoichiometric bulk magnetite is a_0 = 8.3918 Å, but for smaller particles, it tends to decrease [15]. Mössbauer results indicate oxidation of Fe^{2+} to Fe^{3+}, since the ratios of the areas of octahedral and tetrahedral sites of magnetite nanoparticles (mag) is less than 2.00 (Table 2 and Fig. 4a). There is a gap-free miscibility row between maghemite (γ-Fe_2O_3) and magnetite (Fe_3O_4), which can be written as $Fe_{3-v}\,\square_v\,O_4$ with $0 \leq v \leq 1/3$ and $\square$ as vacancy. Maghemite is reached at v = 1/3. The number of vacancies can be determined from Mössbauer data. From the area ratio x of the octahedral subspectra (O) and tetrahedral subspectra (T) follows that $v = (2 - x)/(5x+6)$ [20]. For sample mag (x = 1.26), v = 0.06. Whether the core contains more magnetite or more maghemite plays no role in the performance of the nanocomposites. The magnetic hysteresis curve of magnetite nanoparticles was recorded at 300 K (room temperature) (Fig. 5a). The paramagnetic contribution is a linear function of the field and does not saturate at the fields usually applied. Therefore, the flat high field part of the hysteresis was interpolated toward the ordinate to give the magnetic saturation (Ms) at the crossing point. The saturation magnetization (Ms) at 300 K is about 70 emu/g (Table 1), close to that reported in the literature for synthesized magnetite nanoparticles with a d_{XRD} of 15 nm [15]. The possible causes of the decrease in Ms, when compared with bulk magnetite (reported in the literature to have Ms of ∼94 emu/g [15]), could be chemical changes on the surface, such as the oxidation shown by the Mössbauer data, and the decreased particle size. The magnetite nanoparticles exhibit a superparamagnetic state at room temperature, which is indicated by the disappearance of hysteresis (zero coercive field, Table 1). In the presence of a magnetic field, the superparamagnetic particles behave like small permanent magnets, so that they form aggregates due to magnetic interaction. Once the applied magnetic field is removed, the magnetic particles retain no residual magnetism at room temperature.

Surface measurement of the magnetite particles via nitrogen gas absorption yielded a Brunauer, Emmett and Teller (BET) surface area (A_s) of 92 m^2/g. A mean particle size of 13 nm was estimated using the relation d_{BET} = $6/\rho A_s$ with the density ρ = 5.1 g/cm^3 for
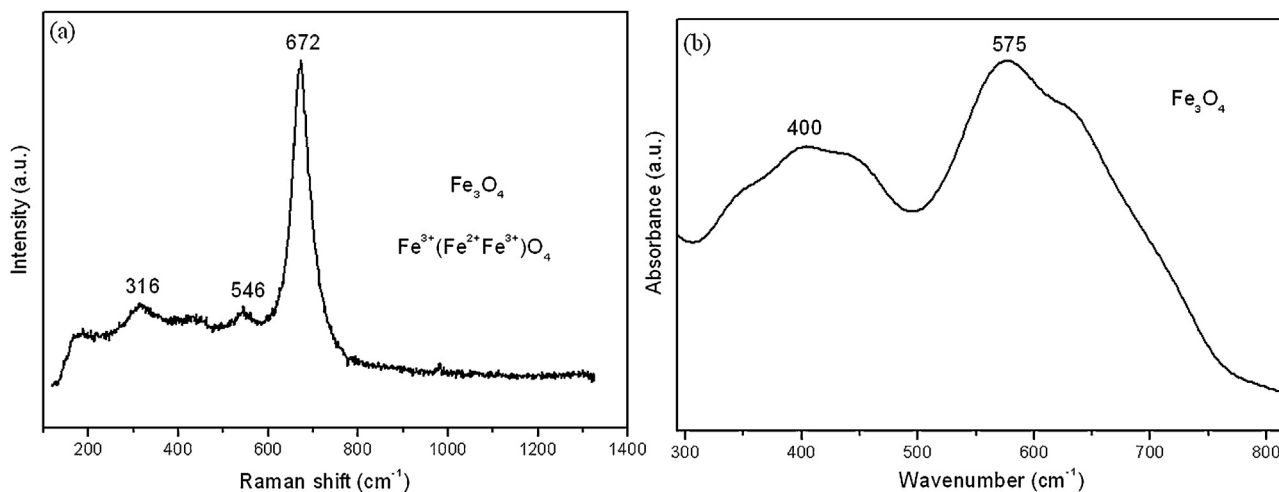

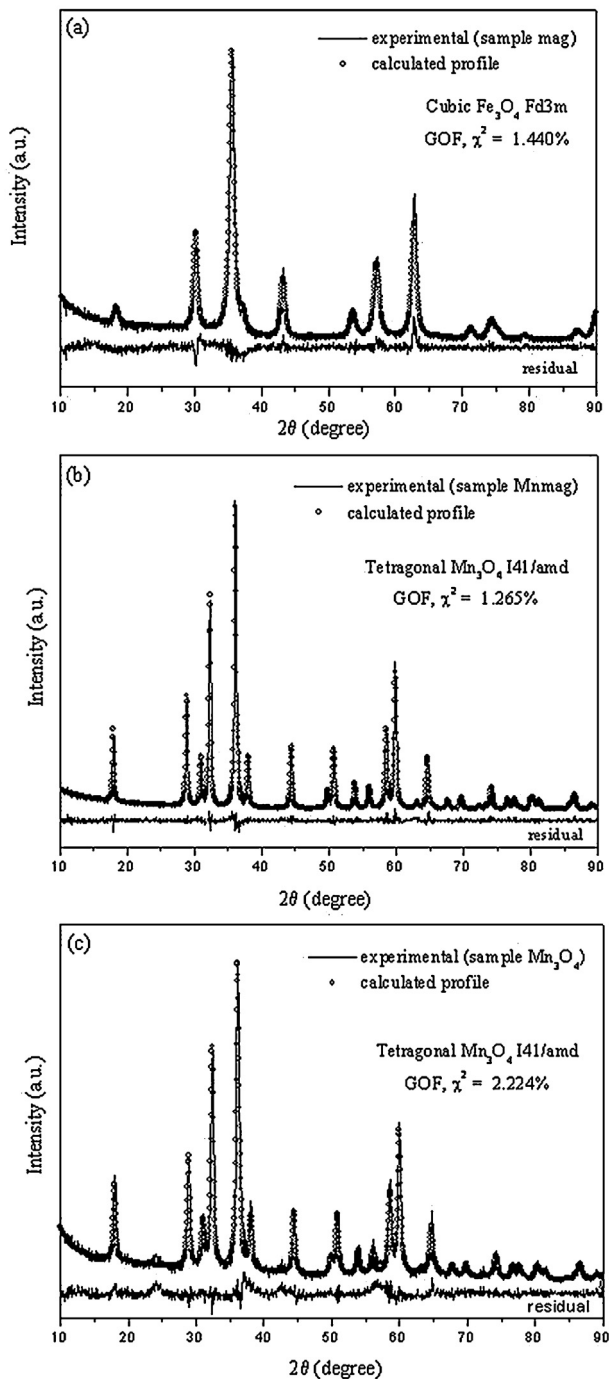**Fig. 1.** (a) Raman and (b) FTIR spectra of synthesized magnetite nanoparticles.

Fig. 2. Powder X-ray diffraction pattern of: (a) synthesized magnetite (mag), (b) synthesized magnetic Mn_3O_4 composite (Mnmag) and (c) Mn_3O_4 particles.

the magnetite nanoparticles (Table 1). The morphology of magnetite nanoparticles with TEM images indicated aggregated, octahedral magnetite nanoparticles with an average size of about 10 nm (Fig. 3a).

Table 1
BET surface areas (S_{BET}), BET diameter (d_{BET}), crystallite size (d_{XRD}), saturation magnetization (M_S) and coercive field (H_C) of the samples.

Sample	S_{BET} (m²/g)	d_{BET} (nm)	d_{XRD} (nm)	M_S (emu/g)	H_C (Oe)
mag	92	13	13	70	0
Mnmag	40	30	27	3.75	0
Mn_3O_4	54	23	21	–	–

The synthesis of Mn_3O_4 in the presence (Mnmag) and absence of magnetite is confirmed by the presence of diffraction peaks corresponding to a tetragonal structure of Mn_3O_4. Rietveld refinement of the structure in the tetragonal space group, I41/amd, shows the following cell parameters: lattice constants, $a = b = 5.7639$ Å, $c = 9.4650$ Å and cell volume, $V = 314.449$ Å³ for the composite and lattice constants, $a = b = 5.7586$ Å, $c = 9.4462$ Å and cell volume, $V = 313.229$ Å³ for Mn_3O_4 nanoparticles (Fig. 2b). The Mnmag sample presents crystallite size d_{XRD} of 27 nm and mean particle size d_{BET} of 30 nm, while Mn_3O_4 particles sample presents crystallite size d_{XRD} of 21 nm and mean particle size d_{BET} of 23 nm (Table 1). The synthesis in the presence of magnetite favors the formation of a pure, highly ordered Mn_3O_4 material [21]. Mössbauer results indicate oxidation of Fe^{2+} to Fe^{3+}, since the ratios of the areas of octahedral and tetrahedral sites of the Mnmag composite is $x = 1.31$, with $v = 0.06$ (Table 2 and Fig. 4b). Oxidation does not compromise magnetic separation since the composite dispersed in water solution can be separated from water by using magnets (Fig. 6). Moreover, the v values for the composite and magnetite nanoparticles are the same, indicating that the composite synthesis does not compromise the magnetite nanoparticles. The composite's reduced M_S (3.75 emu/g) can be understood as a result of the presence of Mn_3O_4 (Fig. 5b). The TEM image of the composite shows particles with dominantly octahedral morphology, and diameters ranging from 10 to 50 nm (Fig. 3b). The punctual EDS spectra were taken around the particles seen in the image. The Fe-peaks were not identified in the EDS spectra (data not shown). Since we are forming agglomerates and small amounts of Fe are being investigated in the presence of large amounts of Mn (Mn Kβ is very close to Fe Kα), it was not possible to distinguish the Fe_3O_4 particles from the Mn_3O_4 particles by EDS. High Resolution Transmission Electron Microscopy (HRTEM) could also not be used to distinguish the two phases. The main issue in performing HRTEM is that, as seen in the diffraction patterns, the $d<h\,k\,l>$ for the Mn_3O_4 and Fe_3O_4 crystalline systems are very close and many of them coincide. We cannot know the exact crystallographic direction just based on the HRTEM image, because as the interplanar distances are similar in both crystals, it is not possible to distinguish the crystals accurately. In summary, the interplanar spacing measured in the high resolution image coincides with the $d<h\,k\,l>$ of the crystal only if the crystal axis is aligned in the $<h\,k\,l>$ zone. If we were able to identify Fe_3O_4 by selected area diffraction (SEAD), we could align the particles and find an image that corresponds to the plane $<1\,1\,1>$. However, Fe_3O_4 was not identified, neither by EDS nor by SEAD (data not shown).

Significant agglomeration took place during synthesis and the Mn_3O_4 and Fe_3O_4 particles appear as large agglomerates, with the Fe_3O_4 particles being covered by Mn_3O_4 particles. Lack of magnetite (Fe_3O_4) contribution in the diffractogram, along with the BET surface area value of the composite, 40 m²/g (approaching to that of Mn_3O_4 particles, 54 m²/g – Table 1), confirm that the Mn_3O_4 particles are covering the Fe_3O_4 particles.

3.2. Degradation of MB

Decolorization of MB by Mn_3O_4 nanoparticles and Mn_3O_4 magnetic composites (Mnmag) was investigated spectroscopically through UV–visible (UV–vis) spectroscopy and the discoloration efficiency (%) of the samples at different reaction times was calculated according to the following equation (Eq. (2)):

$$\text{Discoloration efficiency}(\%) = 100 \times \frac{A_0(\lambda_{max}) - A(\lambda_{max})}{A_0(\lambda_{max})} \quad (2)$$

with $A_0(\lambda_{max})$: initial absorbance and $A_0(\lambda_{max})$: absorbance at time t of MB.
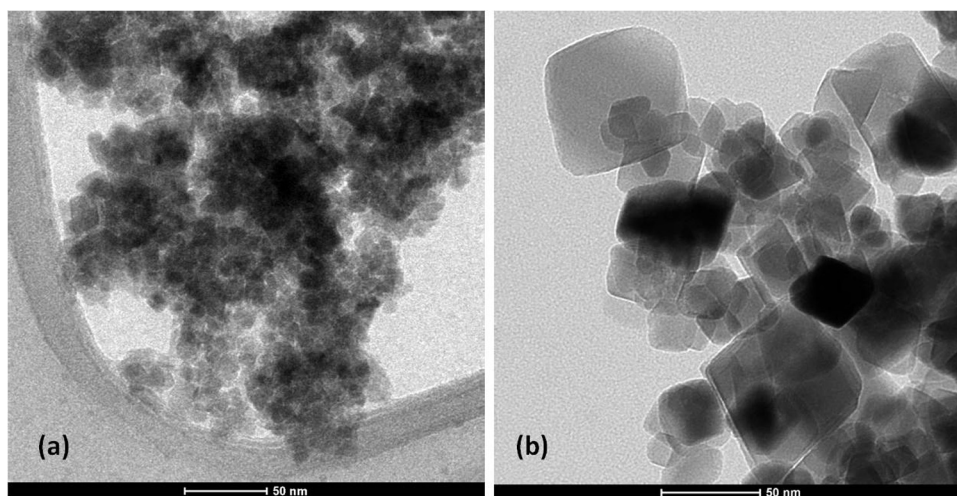
Fig. 3. TEM images of the (a) magnetite particles (mag) and the (b) composite (Mnmag).

Table 2
Mössbauer hyperfine parameters of magnetite nanoparticles (mag) and magnetic composite (Mnmag) at 77 K.

Magnetite			Composite		
	mag (O)	mag (T)		mag (O)	mag (T)
IS (mm/s)	0.45	0.42	IS (mm/s)	0.47	0.40
QS (mm/s)	0.00	−0.01	QS (mm/s)	−0.03	−0.01
B_{HF} (T)	52.2	49.2	B_{HF} (T)	52.4	50.1
Area (%)	55.8	44.2	Area (%)	56.8	43.2
$A_{(O)}/A_{(T)}$ (x)	1.26	$A_{(O)}/A_{(T)}$ (x)		1.31	

IS, isomer shift; QS, quadrupole splitting; B_{HF}, hyperfine field; T, tetrahedral sites; O, octahedral sites.

According to the literature, it has been well established that oxidative degradation of organic matter by Mn oxides proceeds via a surface mechanism – the organic compound is adsorbed on the surface of Mn oxides to form a surface precursor complex. Electron transfer then occurs from surface bound organic reductant to the surface bound Mn^{3+}/Mn^{4+}, followed by the release of organic oxidation products and Mn^{2+} arising from reductive dissolution of Mn oxides [7,9]. Zaied et al. (2011) use thin layers of birnessite (manganese dioxide) to degrade methylene blue (MB) contained in aqueous solutions and revealed the presence of intermediate

reaction products (azure A (AA), azure B (AB), azure C (AC), and thionine (Th) – Fig. 7) during interaction [9]. The characteristic UV–vis λ_{max} of AA, AB, AC, and Th were identified as 628, 638, 618 and 601 nm, respectively [9]. The following equations (Eqs. (3)–(7)) show the Mn_3O_4 reductive dissolution reaction and N-demethylation reactions of MB and its derivatives. Mn_3O_4 favors electron transfers leading to the N-demethylation oxidative reaction of MB to form colored intermediary compounds:
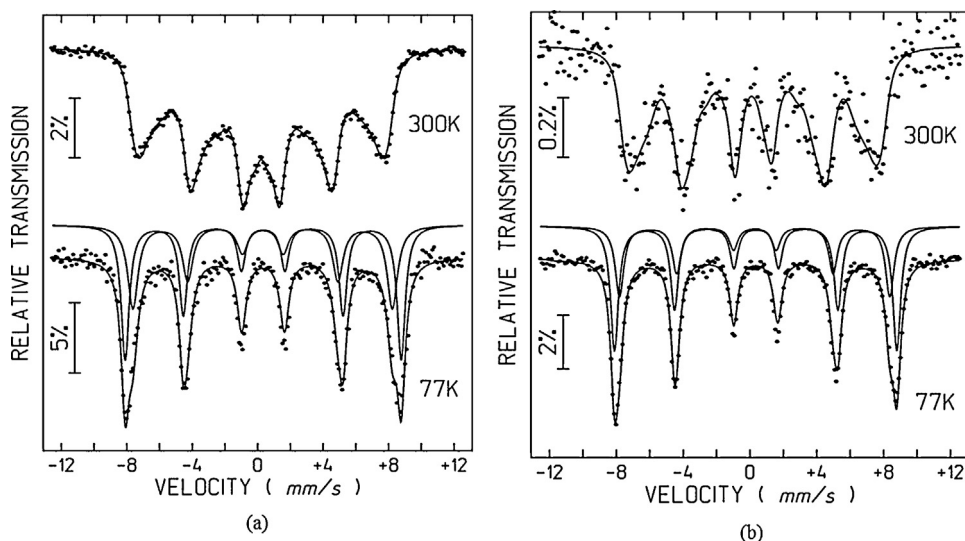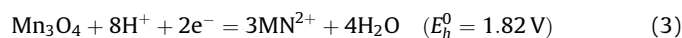
$$Mn_3O_4 + 8H^+ + 2e^- = 3MN^{2+} + 4H_2O \quad (E_h^0 = 1.82\,V) \tag{3}$$

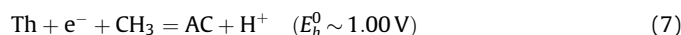**Fig. 4.** Mössbauer spectra of (a) magnetite nanoparticles and the magnetic composite (Mnmag) measured at 77 K.
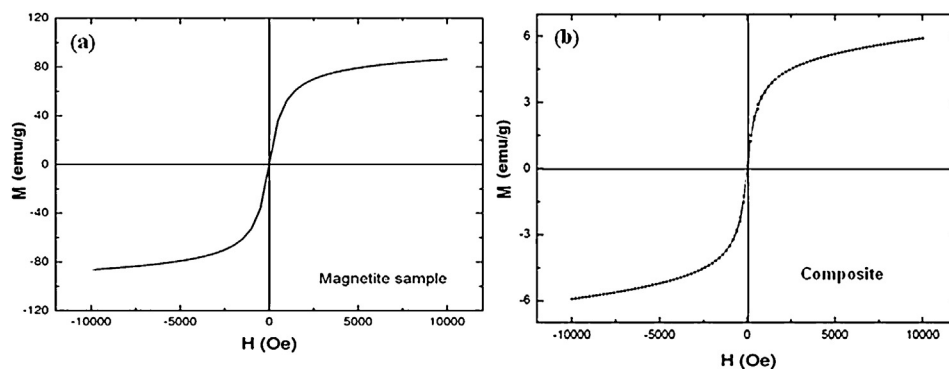
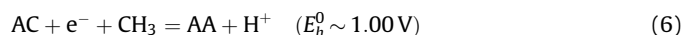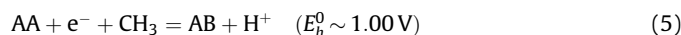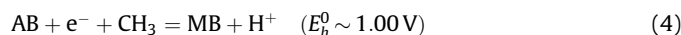**Fig. 5.** Room temperature magnetization curves of: (a) synthesized magnetite (mag) and (b) magnetic Mn_3O_4 composite (Mnmag).

$$AB + e^- + CH_3 = MB + H^+ \quad (E_h^0 \sim 1.00\,V) \tag{4}$$

$$AA + e^- + CH_3 = AB + H^+ \quad (E_h^0 \sim 1.00\,V) \tag{5}$$

$$AC + e^- + CH_3 = AA + H^+ \quad (E_h^0 \sim 1.00\,V) \tag{6}$$

$$Th + e^- + CH_3 = AC + H^+ \quad (E_h^0 \sim 1.00\,V) \tag{7}$$

UV–vis spectra of the 1.4×10^{-5} mol/L MB solution before and after charging Mn_3O_4 nanoparticles and Mnmag suspensions (0.7 and 1.4 g/L) at pH 3.0 are shown in Fig. 8. Spectra of dye solution, before adding the solids, clearly exhibit the characteristic λ_{max} (maximum wavelength) peak of MB at 667 nm. As soon as the solids are added to the dye solution at pH 3.0, the peaks changed position and intensity indicating that MB was oxidized by Mn_3O_4. For Mn_3O_4 nanoparticles (Fig. 8a), after 5 min of reaction with MB, λ_{max} becomes 634 nm, which is close to λ_{max} of AB. After 10 min, λ_{max} shifts to 627 nm, which is close to λ_{max} of AA. After 15 min and 20 min, λ_{max} shifts to 613 and 612 nm, close to λ_{max} of AC. After 30 min until 180 min, λ_{max} remains constant at $\sim$600 nm, which is close to λ_{max} of Th. For 0.7 g/L Mnmag (Fig. 8b), MB is oxidized only after 20 min, when it is transformed to AB. Then, MB is transformed to AA after 30 min, to AC after 60 min and to Th after 90 min. For 1.4 g/L Mnmag (Fig. 8c), MB is oxidized to AB after 10 min and to Th after 60 min. The UV–vis spectra of the 1.4×10^{-5} mol/L MB solution before and after charging Mn_3O_4 nanoparticles suspension (0.7 g/L) at pH 4.0 and pH 6.0 shows that the MB peaks only changed in intensity, remaining in the same positions over time (Fig. 9).
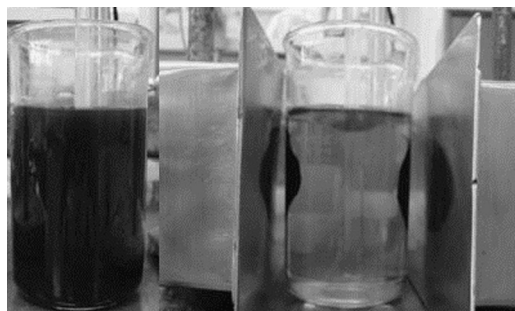
Fig. 10a shows the discoloration efficiency (%) (Eq. (2)) versus time for Mn_3O_4 nanoparticles and Mnmag suspensions at pH 3.0. For 0.7 g/L Mn_3O_4 nanoparticles, 86% of color disappeared after 60 min and remained constant until 180 min. For 0.7 g/L Mnmag, 83% of color disappeared after 90 min and remained constant until 180 min. For 1.4 g/L Mnmag, 85% of color disappeared after 60 min and remained constant until 180 min. When comparing to the literature, these results are similar to the ones found for ZnS/CdS composites (85%) and hollow CdS nanospheres (87%); higher than the ones found for commercial anatase (73%), ZnO (60%), N-CdS (29%), ZnS (27%) and photolysis only (21%); and lower than the ones found for CdS – 6, 8, 18 (above 96%) and G-ZnO (100%) [22–26]. For Mn_3O_4 nanoparticles, at pH 4.0 and pH 6.0, the discoloration remained constant at $\sim$50% (Fig. 10b).

The results show that at pH 4.0 and pH 6.0, MB was not oxidized by Mn_3O_4 (Figs. 9 and 10b), indicating that the role of acid is very important in the decolorization reaction, which is explained by the H^+ dependent Mn_3O_4 reductive reaction (Eq. (3)). Furthermore, the oxidative reaction is three times faster (Fig. 8) and discoloration is slightly higher (Fig. 10a) for the 0.7 g/L Mn_3O_4 nanoparticles than for 0.7 g/L Mnmag suspension. However, when the Mnmag concentration is doubled (1.4 g/L), the oxidation reaction rate and discoloration increase (Figs. 8c and 10a). Therefore, the reduction in the oxidative reaction rate and discoloration for 0.7 g/L Mnmag is explained by the lower amount of Mn_3O_4 in the composite.

Methanol (MeOH) was used to dissolve organic compounds present onto the solids after interaction aimed at identifying them. The solids were immersed for 24 h. The organic compounds were identified by UV–vis spectroscopy. Fig. 11 presents the absorbance
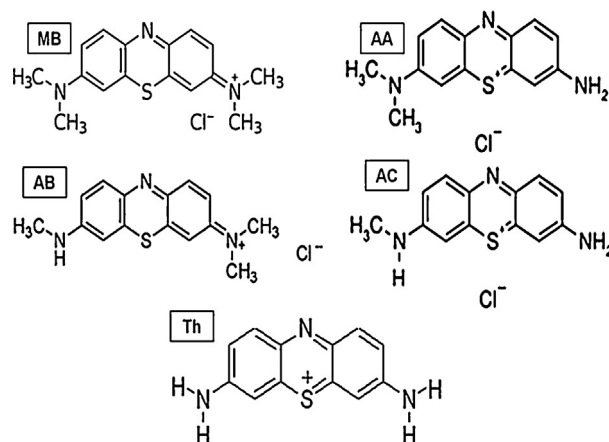

Fig. 6. Magnetic Mn_3O_4 composite (Mnmag) dispersed water solution and magnetic separation.

Fig. 7. Methylene blue (MB) and its N-demethylated derivatives.
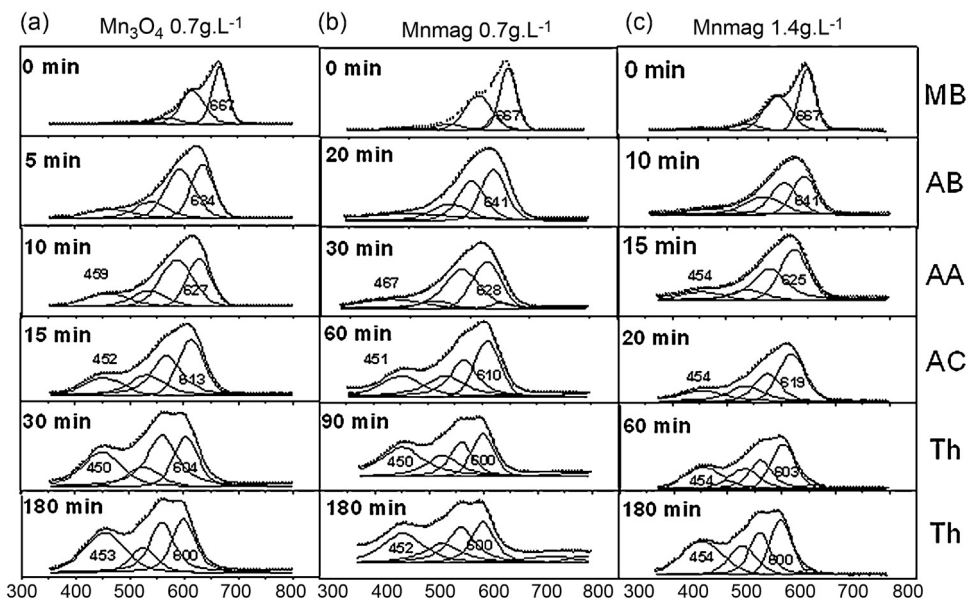
Fig. 8. UV–vis spectra peak fitting of 1.4×10^{-5} mol/L MB solution before and after charging (a) Mn_3O_4 nanoparticles (0.7 g/L) and the magnetic Mn_3O_4 composite (Mnmag) (b) 0.7 g/L and (c) 1.4 g/L suspensions at pH 3.0.
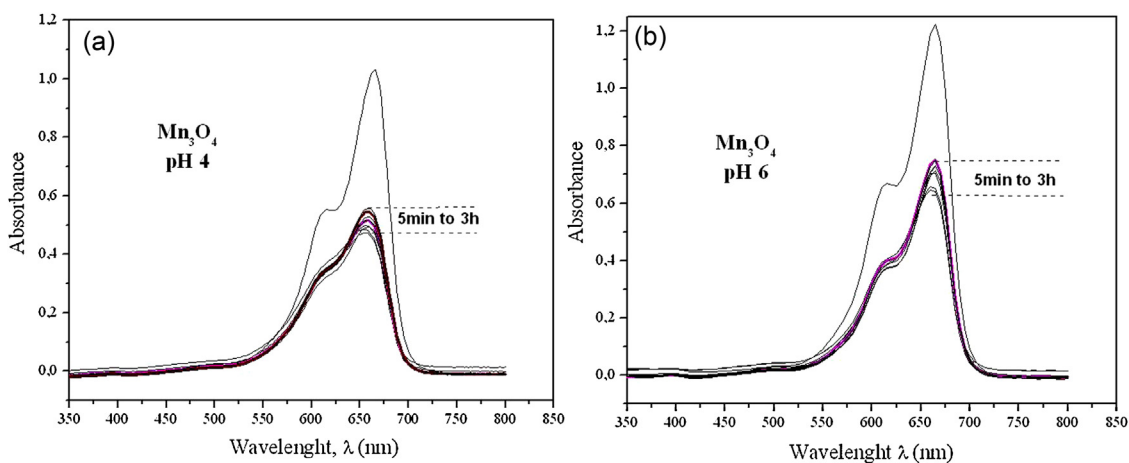

Fig. 9. UV–vis spectra of 1.4×10^{-5} mol/L MB solution before and after charging Mn_3O_4 nanoparticles suspension (0.7 g/L) at (a) pH 4.0 and (b) pH 6.0.
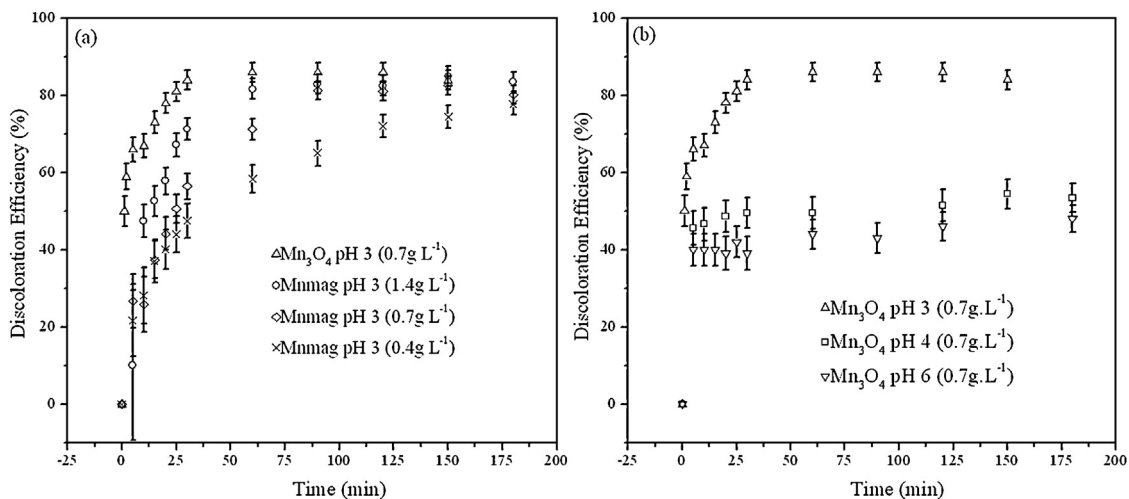

Fig. 10. Discoloration efficiency (%) versus time of 1.4×10^{-5} mol/L MB solution in interaction with (a) 0.4 g/L, 0.7 g/L and 1.4 g/L Mnmag suspensions at pH 3.0, and (b) with 0.7 g/L Mn_3O_4 nanoparticles at pH 3.0, 4.0 and 6.0.
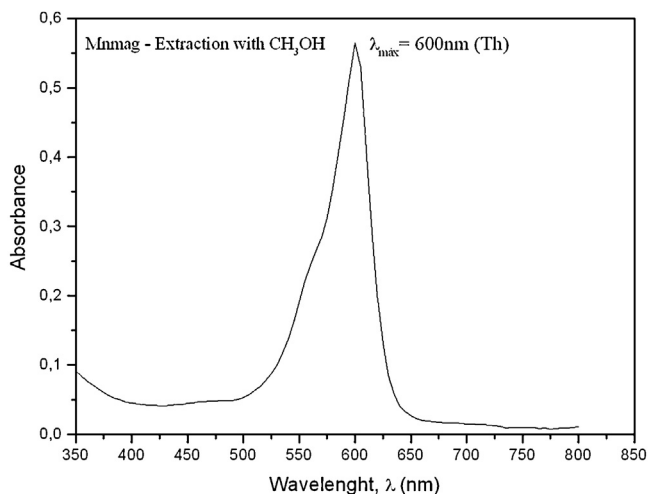
Fig. 11. UV–vis spectrum of MeOH solution after 24 h of leaching reaction of Mnmag sample which have interacted with MB solution containing 1.4×10^{-5} mol/L during 48 h.

measurements obtained with the MeOH solution. The measured value of λ_{max} = 600 nm is the characteristic λ_{max} of thionine [9], indicating that the MB fully demethylated derivative is the adsorbed organic compound after MB oxidation.

Thionine was obtained as the end product of the degradation of methylene blue, but its presence in the medium is also undesirable. In this aspect, the attempt to increase the pH of the final solution to values close to 10 proved to be satisfactory, reducing part of the thionine concentration in the solution. Although aliquots were taken at different time intervals for 1 h, the reduction occurred in the first 5 min after raising the pH and remained constant thereafter. We observed an additional 8% reduction in absorbance value of the peak of thionine (data not shown) after increasing pH as described. However, ways to promote the total elimination of the organic compounds remaining in the solution are still being investigated.

4. Conclusions

Mn$_3$O$_4$–Fe$_3$O$_4$ nanocomposites were synthesized via co-precipitation of Mn$_3$O$_4$ in the presence of synthesized magnetite nanoparticles. Raman and FTIR spectroscopy results show the main magnetite bands confirming that the magnetite particles synthesis was well accomplished. The synthesized magnetite particles with 70 emu/g of saturation magnetization and a superparamagnetic state at room temperature present a cubic spinel structure with a_0 = 8.3617 Å, and a particle diameter of ~10 nm. The Mn$_3$O$_4$ synthesis in the presence of these magnetite nanoparticles favors the formation of a pure, highly ordered magnetic Mn$_3$O$_4$ composite. The composite is superparamagnetic at room temperature and can be separated by an external magnetic field. The Mn$_3$O$_4$ magnetic composite is capable of catalyzing the complete N-demethylation of MB, forming thionine as the final product and removing 93% of the dye.

Appendix A. Supplementary data

Supplementary material related to this article can be found, in the online version, at http://dx.doi.org/10.1016/j.materresbull.2013.09.039.

References

[1] P. Grau, Water Sci. Technol. 24 (1) (1991) 97–103.
[2] E.R. Stobhe, B.A.D. Boer, J.W. Geus, Catal. Today 47 (1999) 161–167.
[3] L. Xu, C. Xu, M. Zhao, Y. Qiu, G.D. Sheng, Water Res. 42 (2008) 5038–5044.
[4] K. Abdelazez, M. Ahmed, Q. Zeng, K. Wu, K. Huang, J. Solid State Chem. 183 (2010) 744–751.
[5] S.C. Kima, W.G. Shim, Appl. Catal. B: Environ. 98 (2010) 180–185.
[6] T. Rhadfia, J.-Y. Piquemal, L. Sicard, F. Herbst, E. Briot, M. Benedetti, A. Atlamsani, Appl. Catal. A: Gen. 386 (2010) 132–139.
[7] A.-N. Chowdhury, Md.S. Azam, Md. Aktaruzzaman, A. Rahim, J. Hazard. Mater. 172 (2009) 1229–1235.
[8] A. Katafias, J. Fenska, Transit. Metal Chem. 36 (2011) 801–809.
[9] M. Zaied, S. Peulona, N. Bellakhal, B. Desmazièresd, A. Chausséa, Appl. Catal. B: Environ. 101 (2011) 441–450.
[10] J. Qu, J. Environ. Sci. 20 (2008) 1–13.
[11] C.A.C. Rosas, M. Franzreb, F. Valenzuela, W.H. Höll, React. Funct. Polym. 70 (2010) 516–520.
[12] H. Chen, P.K. Chu, J. He, T. Hu, M. Yang, J. Colloid Interface Sci. 359 (2011) 68–74.
[13] T.M. Dlugosch, International Institute for Infrastructural Hydraulic and Environmental Engineering, 2001 (M.Sc. Thesis).
[14] Y. Zhai, J. Zhai, M. Zhou, S. Dong, J. Mater. Chem. 19 (2009) 7030–7035.
[15] J. Mürbe, A. Rechtenbach, J. Töpfer, Mater. Chem. Phys. 110 (2–3) (2008) 426–433.
[16] L.C.A. Oliveira, D.I. Petkowicz, A. Smaniotto, S.B.C. Pergher, Water Res. 38 (2004) 3699–3704.
[17] X.J. Peng, Z.K. Luan, Z.C. Di, Z.G. Zhang, C.L. Zhu, Carbon 43 (2005) 855–894.
[18] H.-D. Pfannes, J.H. Dias Filho, R. Magalhães-Paniago, J.L. Lòpez, R. Paniago, Braz. J. Phys. 31 (2001) 409–417.
[19] A.M. Jubb, H.C. Allen, ACS Appl. Mater. Interfaces 2 (10) (2010) 2804–2812.
[20] A. Ramdani, J. Steinmetz, C. Gleitzer, J.M.D. Coey, J.M. Friedt, J. Phys. Chem. Solids 48 (1987) 217–228.
[21] Y.F. Han, F.X. Chen, Z.Y. Zhong, K. Ramesh, L.W. Chen, E. Widjaja, J. Phys. Chem. B 110 (2006) 24450–24456.
[22] S. Liu, H. Li, L. Yan, Mater. Res. Bull. 48 (2013) 3328–3334.
[23] W.-M. Zhang, Y.-Q. Jiang, X.-Y. Cao, M. Chen, D.-L. Ge, Z.-X. Sun, Mater. Res. Bull. (2013), http://dx.doi.org/10.1016/j.materresbull.2013.07.008.
[24] G. Lin, J. Zheng, R. Xu, J. Phys. Chem. C 112 (2008) 7363–7370.
[25] A. Wei, L. Xiong, L. Sun, Y. Liu, W. Li, W. Lai, X. Liu, L. Wang, W. Huang, X. Dong, Mater. Res. Bull. 48 (2013) 2855–2860.
[26] X. Li, Y. Gao, L. Yu, L. Zheng, J. Solid State Chem. 183 (2010) 1423–1432.